Retrieval and Evaluation of Ice Water Content from the Airborne Wyoming Cloud Radar in Orographic Wintertime Clouds during SNOWIE

MIN DENG,[a,b] JEFFREY FRENCH,[a] BART GEERTS,[a] SAMUEL HAIMOV,[a] LARRY OOLMAN,[a] DAVE PLUMMER,[a]
AND ZHIEN WANG[b,c]

[a] *Department of Atmospheric Science, University of Wyoming, Laramie, Wyoming*
[b] *Laboratory for Atmospheric and Space Physics, University of Colorado Boulder, Boulder, Colorado*
[c] *Department of Atmospheric and Oceanic Sciences, University of Colorado Boulder, Boulder, Colorado*

(Manuscript received 28 June 2021, in final form 4 November 2021)

ABSTRACT: As part of the analysis following the Seeded and Natural Orographic Wintertime Storms (SNOWIE) project, the ice water content (IWC) in ice and mixed-phase clouds is retrieved from airborne Wyoming Cloud Radar (WCR) measurements aboard the University of Wyoming King Air (UWKA), which has a suite of integrated in situ IWC, optical array probes, and remote sensing measurements, and it provides a unique dataset for this algorithm development and evaluation. A sensitivity study with different idealized ice particle habits shows that the retrieved IWC with aggregate ice particle habit agrees the best with the in situ measurement, especially in ice or ice-dominated mixed-phase clouds with a correlation coefficient (rr) of 0.91 and a bias of close to 0. For mixed-phase clouds with ice fraction ratio less than 0.8, the variances of IWC estimates increase (rr = 0.76) and the retrieved mean IWC is larger than in situ IWC by a factor of 2. This is found to be related to the uncertainty of in situ measurements, the large cloud inhomogeneity, and the retrieval assumption uncertainty. The simulated reflectivity Ze and IWC relationships assuming three idealized ice particle habits and measured particle size distributions show that hexagonal columns with the same Ze have a lower IWC than aggregates, whose Ze–IWC relation is more consistent with the observed WCR Ze and in situ IWC relation in those clouds. The 2D stereo probe (2DS) images also indicate that ice particle habit transition occurs in orographic mixed-phase clouds; hence, the retrieved IWC assuming modified gamma particle size distribution (PSD) of aggregate particles tends to have a greater bias in this kind of clouds.

KEYWORDS: Aircraft observations; Algorithms; Cloud retrieval; Radars/radar observations; Remote sensing

1. Introduction

The Seeded and Natural Orographic Wintertime Storms (SNOWIE; French et al. 2018; Tessendorf et al. 2019) project in January–March 2017 was designed to investigate the impact of glaciogenic cloud seeding in the context of natural orographic precipitation processes, focusing on ice initiation, snow growth, and the impacts of orography on the development of precipitation in wintertime clouds. The western slopes of the mountains in the western United States typically experience upslope flow and a clean Pacific moisture supply in the cold season, favoring the development of layers of high supercooled water (SLW) concentrations, suitable for glaciogenic cloud seeding. On the scale of individual terrain ridges, updrafts associated with vertically propagating waves may enhance the amount of SLW and improve a cloud's seedability. On an even smaller scale, orographic clouds often encounter locally enhanced wind shear leading to Kelvin–Helmholtz waves (Geerts et al. 2011; Keeleret al. 2016; Grasmick and Geerts 2020). The primary scientific objectives of SNOWIE are 1) to evaluate the role of dynamical and microphysical processes that form and enhance clouds and precipitation and the impact of terrain on the formation, growth, and fallout of ice crystals in winter storms and 2) to describe and quantify the impact of airborne and ground-based glaciogenic seeding on hydrometeor growth processes and precipitation in wintertime orographic clouds.

To meet these objectives, measurements were collected with a suite of in situ instruments including a forward scattering cloud droplet probe (CDP) and multiple optical array probes (OAP) for measuring cloud and precipitation hydrometeors, liquid and total-condensed bulk water content sensors, and remote sensors including the Wyoming Cloud Radar (WCR) and Wyoming Cloud Lidar (WCL; Wang et al. 2012) on board the University of Wyoming King Air (UWKA) research aircraft. The UWKA penetrated orographic clouds prior to, during, and after seeding, generally at altitudes corresponding to in-cloud temperatures between −8° and −20°C with the goal of obtaining direct measurements within seeded clouds and investigating the microphysical evolution of both seeded and natural clouds. More details of the experimental design are provided by Tessendorf et al. (2019).

As stated in Rauber et al. (2019), cloud seeding is a dynamic process of converting supercooled water to ice, in such a manner that newly created ice particles can grow and fall to the ground as additional snow on a specified target area. The in situ IWC measurement at flight level could not show such vertical growth in the seeded clouds. So far, the analysis of microphysical response from seeding orographic clouds during the SNOWIE project (Tessendorf et al. 2019;

Denotes content that is immediately available upon publication as open access.

Corresponding author: Min Deng, mdeng2@uwyo.edu

DOI: 10.1175/JTECH-D-21-0085.1

Friedrich et al. 2021) is based on the Ze profiles instead of direct cloud microphysical properties. To extend the detailed in situ microphysical measurements to locations above and below flight level, we adopt the three Doppler radar moments retrieval algorithm (Deng and Mace 2006) to the UWKA WCR observations to retrieve the profiles of IWC, mean air vertical motion, and effective radius. In this study, we focus on the IWC evaluation with the in situ measurement. A brief description of the relevant in situ and remote sensing instruments used in SNOWIE and their measurement capabilities are provided in section 2. Section 3 describes the IWC retrieval algorithm. In section 4, the retrieved IWC is evaluated with in situ IWC and OAP measurement. The summary is given in section 5.

2. UWKA data

The WCR (Haimov and Rodi 2013) is a Doppler radar operating at 95 GHz. For the SNOWIE experiment it was mounted on board the UWKA main body and provided measurements of radar reflectivity factor Ze, Doppler velocity Vd, and Doppler spectral width. The signal was transmitted and received by three fixed-mounted antennas directed toward near zenith (“zenith” antenna), near nadir (“nadir” antenna), and ~30° forward of nadir. In this study only zenith and nadir antenna products are utilized. The WCR reflectivity is calibrated using corner reflectors, and its uncertainty is about 2 dB.

The WCR measured Doppler velocity (Vd) contains main contributions from the hydrometeor, the aircraft motion, and horizontal wind components in the radar resolution volume. To keep the effect of aircraft motion and horizontal wind on Vd to the minimum, we use observations from straight and level flight legs during the SNOWIE project to retrieve IWC within an optimization framework. The zenith and nadir antennas are mounted on the aircraft in a way that minimizes the departure of the antenna beam-pointing vectors from zenith and nadir in straight and level flight legs. Any deviation of the antenna beam-pointing vectors from being orthogonal with respect to the aircraft velocity vector induces contribution of the aircraft motion into the measured Doppler velocity. To remove this contribution, first, the fixed beam-pointing vector of the nadir antenna is calibrated using Doppler data from ground returns (Haimov and Rodi 2013). The zenith beam-pointing vector is cross calibrated with the downward beam. Once the accurate beam-pointing vector is determined, the aircraft motion contribution is removed using the known aircraft velocity vector and the aircraft attitude. The maximum root-mean-square error in the calibrated nadir and zenith beam-pointing angles for SNOWIE is estimated to be on the order of 0.1° with residual aircraft motion contribution in the corrected Doppler velocity not exceeding 0.1–0.3 m s^{-1}.

Measured Doppler velocity after correcting for the aircraft motion correction represents the mean vertical air motion, hydrometeor terminal velocity, and horizontal wind contribution. If the radar beam is strictly vertical there is no horizontal wind contribution. However, given that an aircraft, even for smooth straight and leveled flights, frequently experiences small changes in attitude, horizontal wind has some component included in the measured Doppler. This contribution is more significant under strong winds aloft and/or when the aircraft experiences turbulence. We have used wind data from a nearby rawinsonde to remove the horizontal wind contributions from the Doppler data used in this paper. Based on the comparison of retrieved air motion between along- and opposite-wind flights (figure not shown), the horizontal wind contamination is generally less than 0.1 m s^{-1}.

The downward-pointing WCL II (operating wavelength 351 nm; Wang et al. 2009) is used to obtain the SLW information with the vertical profiles of backscatter power and linear lidar depolarization ratio (LDR) below the aircraft flight level. Lidar backscatter power is stronger in liquid and liquid-dominated mixed-phase clouds than in ice clouds because small liquid droplet number concentration is usually much higher than large ice particle concentration. It also attenuates rapidly due to large extinction of liquid droplets (Kikuchi et al. 2021). LDR is defined as the ratio of backscatter power in a perpendicular (cross polarized) channel to backscatter power in a parallel (copolarized) channel for a linearly polarized transmitted light. It is calibrated in the optical laboratory, while its absolute value can be slightly affected by the extra UWKA lidar installation window. The relative value is used for cloud phase identification. Higher backscattering power, smaller LDR values, and quicker signal attenuation indicate the presence of spherical liquid droplets, whereas larger LDR values indicate the presence of nonspherical ice particles (Wang et al. 2012).

The Nevzorov liquid and total water content (LWC–TWC) probe (Korolev et al. 1998; Korolev and Strapp 2002) consists of two different sensors for measurement of TWC and LWC in clouds and fogs, which are fully calculable from the first principle of the heat transfer on the sensor wire, the difference of which yields IWC. The LWC sensor has a half-cylinder shape with 1.5-mm diameter. The TWC sensor is an 8-mm-diameter concave cone, which faces the flow and works as a trap for impacting cloud particles. The Nevzorov probe swivels to align with airflow. The measurements of water content in clouds by hot-wire probes depend on the shape of the collector sensor; airspeed; air pressure and temperature; droplet size distribution; preferred particle size, shape, and density; and local aerodynamic effects around the aircraft, which define the collection efficiency and thus affect the errors in measurements. The LWC efficiency is typically close to unit, but the efficiency for capture and evaporation of ice particles is relatively lower, on the order of 30%–50% by some estimates (Strapp et al. 2005; Korolev et al. 2013a; Leroy et al. 2017a,b).

In the comparison of King probes with Nevzorov probe and constant-temperature T probes (Vidaurre et al. 2011), levels of disagreement between the probes changed during numerous cloud penetrations from less than 20% up to a factor of 2, varying with flight conditions and microphysical structure of the cloud. Discrepancies of up to 0.1 g m^{-3} for LWC measurements of 0.3 g m^{-3} were observed. A comparison of LWC measurements between the Nevzorov and the CDP mounted on the UWKA during SNOWIE indicated results from the

Nevzorov were less by about 20% relative to that calculated from the CDP measurement (Faber et al. 2018). Errors and uncertainty in IWC from the Nevzorov probe measurements are related to errors and uncertainties in both LWC and TWC measurements and it is more difficult to evaluate. The deconvolution in mixed-phase conditions during SNOWIE further exacerbates the IWC error, which requires two sensing wires with differing LWC and IWC efficiencies (Korolev et al. 1998; Brenguier et al. 2013). French and Behringer (2021) manually reprocessed the data using some assumptions since a baseline shift can occur at any time in or out of cloud. We only consider values of IWC larger than 0.05 g m^{-3} in the retrieval evaluation because of the uncertainty.

In situ measurements of hydrometeor size, shape, and concentration for particles with diameters larger than about 50 μm are provided by two OAPs on board the UWKA, a SPEC, Inc., 2D stereo probe (2DS; Lawson et al. 2006) and a PMS 2D precipitation probe (2DP). OAPs image particles as they pass through an illuminated volume and cast a shadow on a linear array of photodiodes. The 2DS is capable of imaging particles with 10-μm resolution across a diode array that is 1.28 mm in length, whereas the coarser resolution of the 2DP (200 μm) operates across a diode array length of 6.4 mm. Data from these OAPs were processed using the University of Illinois OAP Processing Software (UIOPS; Jackson et al. 2014; Finlon et al. 2016). Shattering of larger ice crystals was mitigated using both antishattering tips (Korolev et al. 2013b) on the 2DS and removal of artifacts with short interarrival times within the processing software (Finlon et al. 2016; Field et al. 2006).

For hydrometeors with diameters of less than 50 μm, particle size and concentration are provided by a CDP (Lance 2010; Faber et al. 2018), assuming spherical, liquid particles. In the presence of ice, the CDP often responds with elevated counts in its largest size bins, between 40 and 50 μm; however, the counts due to ice in these larger bins are often several orders of magnitude less than the actual count of liquid droplets in the smaller bins. Data from each of the probes are used to construct size distributions with the number of bins and approximate size range, which are listed in Table 1. The three probes' size ranges overlap and together provide a full particle size distribution for diameters from a few micrometers to several millimeters. At times, the 2DS and 2DP show a poor agreement in their overlap region, likely due to undercounting of particles by the 2DP for its smallest detectable particles. Likewise, at times, the 2DS and CDP show similar disagreement in their overlap range. This as well can be attributed both to under/overcounting as well as mis-sizing by the 2DS for particles that are poorly resolved and may be near the edge of their depth of field.

3. WCR retrieval algorithm

The IWC retrieval algorithm is adopted from the first three-Doppler-moment algorithm of millimeter-wavelength radar Doppler spectrum (Deng and Mace 2006). The algorithm has been applied to Atmospheric Radiation Measurement cloud radar measurements and evaluated with in situ measurements (Deng and Mace 2006) and algorithm intercomparison (Zhao et al. 2012; Comstock et al. 2013). At each range gate, the equivalent radar reflectivity Ze is the zero moment of the measured Doppler spectrum; the measured mean Doppler velocity Vd of the vertically pointing beam represents the sum of the reflectivity-weighted particle fall velocity and the vertical air motion W_m; the Doppler spectrum width is a measurement of the spread of the signal in the Doppler velocity domain. The main sources of this spread within a radar sample volume, for a ground-based profiling radar [as used by Deng and Mace (2006)], are the presence of particles with different terminal velocities and air turbulence. For airborne WCR measurements, the aircraft motion and the finite radar beamwidth cause further broadening of the Doppler spectrum (Skolnik 2008, p. 3.9). In this study, the algorithm utilizes the first two WCR Doppler moments only: radar reflectivity and mean Doppler velocity. The key assumptions in the current algorithm development and application are as follows: 1) Clouds are ice dominated, or at least, the reflectivity can be attributed exclusively to ice particles or snow. 2) The attenuation of reflectivity due to ice is accounted for, but the liquid attenuation is ignored. 3) The ice particles might be rimed under different environments; hence, the particle habits might evolve, which is not taken in consideration in the algorithm since the algorithm assumes a certain particle habit for all clouds.

TABLE 1. Number of bins and approximate size range for each probe used during SNOWIE for IWC evaluation.

Instruments	No. of bins	Size range (μm)
CDP	27	1–50
2DS	128	10–1280
2DP	19	400–6400

a. Optimal estimation framework

The algorithm is built upon an optimal estimation framework (Rodgers 2000; Deng and Mace 2006; Deng et al. 2013). The relationships linking the atmospheric state or cloud properties $\mathbf{x}$ with the radar measurements $\mathbf{y}$ are the forward model; that is,

$$\mathbf{y} = F(\mathbf{x}, b) + \varepsilon, \tag{1}$$

where b are parameters used in the forward model. The inverse problem can be approximated using the Bayes theorem where we maximize the a posteriori likelihood of $\mathbf{x}$ given $\mathbf{y}$. The solution is typically found by iteration by initializing a state vector $\mathbf{x}$ with an a priori ($\mathbf{x}_a$) estimation from extensive in situ measurements or empirical relations or algorithms in the literature. Using Gauss–Newton iteration, an expression for the state vector can be expressed as

$$\mathbf{x}_{i+1} = \mathbf{x}_i + \left(\mathbf{S}_a^{-1} + \mathbf{K}_i^{\mathrm{T}}\mathbf{S}_\varepsilon^{-1}\mathbf{K}_i\right)^{-1}\left\{\mathbf{K}_i^{\mathrm{T}}\mathbf{S}_\varepsilon^{-1}[\mathbf{y} - F(\mathbf{x}_i)] - \mathbf{S}_a^{-1}(\mathbf{x}_i - \mathbf{x}_a)\right\}, \tag{2}$$

where $\mathbf{K}$ is the Jacobian matrix containing the derivatives of each observation with respect to each state vector and $\mathbf{S}_a$ and $\mathbf{S}_\varepsilon$ are the error covariance matrices chosen to limit the

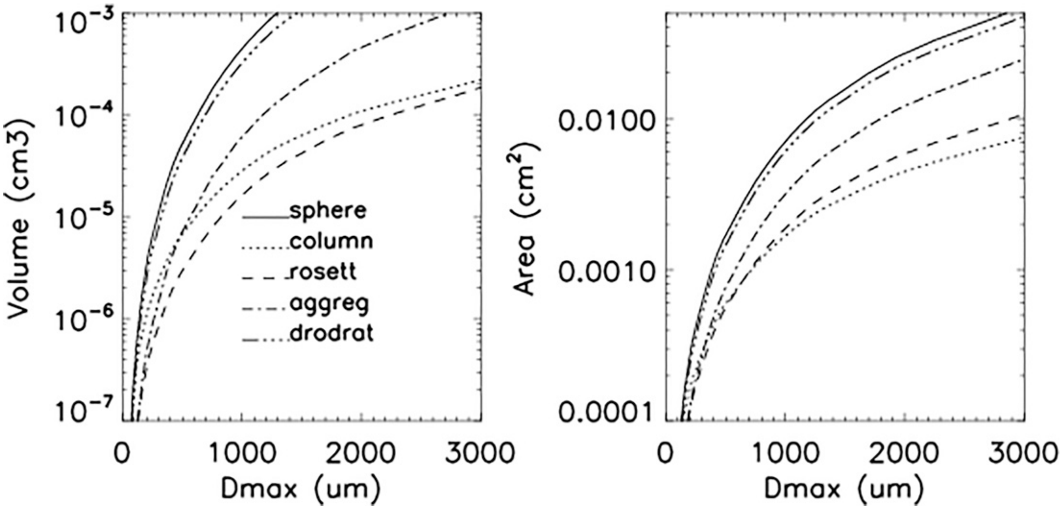

FIG. 1. The (a) parameterized volume and (b) projected area of idealized ice particles as a function of the ice crystal maximum dimension (Dmax) from Table 2 in Yang et al. (2000).

amount of bias of a priori and measurement from the true state vector and ideal measurements, respectively; $\mathbf{S}_a$ is assigned according to the error in the empirical IWC–Ze relationship, and $\mathbf{S}_\varepsilon$ is assigned according to the signal-to-noise ratio in the radar measurement.

b. Radar forward model

The radar forward model relates the atmospheric state parameter with ice particle size distribution $N(D)$ and ice particle habits, which determine the radar backscattering cross section–length $Z(D)$, mass–length $M(D)$, area–length $A(D)$, and terminal velocity–size $V(D)$ relations, to the measured radar reflectivity and Doppler velocity as follows:

$$\mathrm{Ze} = f[N(D),\ Z(D)] \text{ and} \tag{3}$$

$$\mathrm{Vd} = f[N(D), V(D), \mathrm{Wm}]. \tag{4}$$

Here, Wm is the mean air velocity in the WCR sample volume. The bulk ice cloud properties, such as IWC and bulk effective radius re (=3/4 × volume/area; McFarquhar and Heymsfield 1998), can also be found as

$$\mathrm{IWC} = f[N(D), M(D)] \text{ and} \tag{5}$$

$$\mathrm{re} = f[N(D), M(D), A(D)]. \tag{6}$$

The $N(D)$, $Z(D)$, $M(D)$, and $V(D)$ relations compose the ice microphysical model (Deng and Mace 2006). The retrieval of ice properties is sensitive to $N(D)$. For this study, we follow the first-order modified gamma distribution assumption in Deng and Mace (2006). Instead of power-law relations of $Z(D)$, $M(D)$, and $V(D)$ as in Deng and Mace (2006), in this study we use the single-scattering properties of idealized ice particle habits computed from the discrete dipole approximation method in Hong (2007) and Yang et al. (2000), which provided the calculation of backscattering cross section, extinction cross section, volume, and area of a single particle for randomly oriented spherical, hexagonal column, bullet rosette, aggregates, and droxtal-shaped ice particles with maximum length ranging from 2 to 10 500 μm. Figure 1 shows the volume and area of these five ice particle habits. For particles with the same maximum dimension (D or Dmax), the spherical ice particles have the maximum volume and area, followed by droxtal, aggregates, and bullet rosette. The volume of solid hexagonal columns is less than aggregates, and their areas are less than bullet rosettes for particles with Dmax larger than about 500 μm. The change is related to the segmented functions of aspect ratio for columns (Yang et al. 2000).

Using the mass–length and area–length relations of idealized ice particles, we can derive the particle terminal velocity V_t following Mitchell (1996) and Heymsfield and Iaquinta (2000):

$$V_t = \left(\frac{2mg}{\rho_a A C_D}\right)^{1/2},$$

where ρ_a is the air density, m and A are the particle mass and surface area, g is the gravitational acceleration, and C_D is the air drag force coefficient. In practice, V_t is often calculated by defining a term known as the Best number X, which has no dependence on V_t:

$$X = C_D \mathrm{Re}^2 = \frac{2mg\rho_a D^2}{A\eta^2},$$

where η is the dynamic viscosity and Re is the Reynolds number ($=\rho_a V_t D/\eta$). The Re–X power laws are fitted for four X ranges in Mitchell (1996), which represent four flow regimes, that is, viscous flow; laminar, axisymmetric flow; varying degrees of eddy formation downstream; and rapid eddy shedding with turbulence downstream.

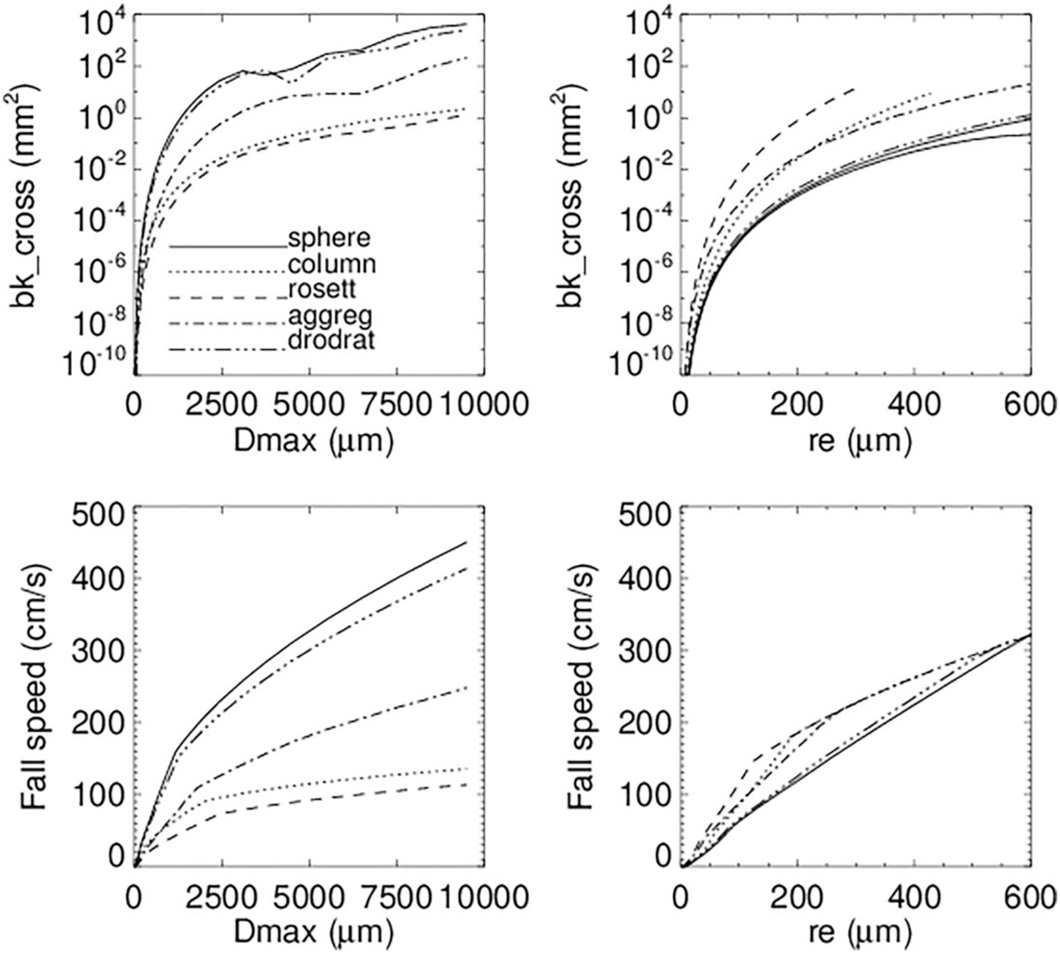

FIG. 2. Parameterized backscattering cross sections (Hong 2007) and particle terminal fall velocities (Mitchell 1996) as a function of Dmax and effective radius re, respectively, of randomly oriented ice crystal particles.

Shown in Fig. 2 are the single ice particle backscattering cross-sectional area and fall speed as a function of Dmax and re. The backscattering cross sections of the five habits have similar relationships with particle volumes in Fig. 1. However, the relationship between backscattering cross section and re is flipped in terms of habit (i.e., spherical particles have a smaller backscattering cross section and bullet rosettes have the largest). The differences of fall speed across the habits increase as the Dmax increases, but when considering fall speed as a function of re the difference between habits is much less, not exceeding 50 cm s^{-1}. Following a modified gamma size distribution $N(D)$ and assuming a specific particle habit, we can calculate Ze, and the quiescent air Vd as a function of bulk effective radius and IWC and put them into a lookup table (LUT) in the radar forward model to save the computational time in the retrieval algorithm.

c. A priori setup

As shown in Eqs. (3)–(6), the algorithm needs to retrieve IWC, re, and Wm with two measurement (Ze and Vd) constraints, which forms an ill-conditioned problem. Thus, the algorithm will heavily depend on the a priori setup to alleviate the retrieval uncertainty. The a priori estimation of IWC is derived from classical Ze–IWC relationships published in literature (Matrosov et al. 2002, 2003; Heymsfield et al. 2008) for orographic snow.

4. Evaluation of IWC retrieval

In all ice cloud retrieval algorithms, the ice particle habit or mass–length relationship is assumed, and if this assumption deviates from the actual cloud properties, then the retrieval will have large uncertainty. The IWC retrieval is run with three different LUTs assuming hexagonal column, aggregate, or droxtal habits as shown in Fig. 2. For those three LUT runs, we only switch the LUT in the radar forward model and keep a priori estimation the same. The WCR retrieval comparison with the Nevzorov measurements shows that the aggregate LUT run has the best correlation and agreement with the in situ measurements, while retrievals assuming columns and droxtals result in poor correlations and agreements; therefore, the following IWC evaluation is based on the

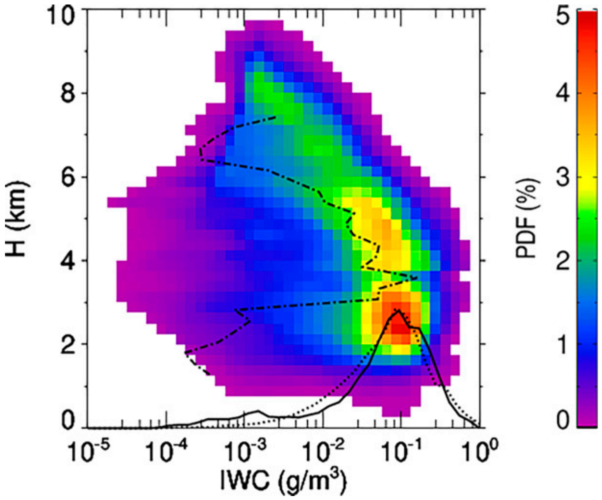

FIG. 3. The PDF of WCR-retrieved IWC over height for the entire SNOWIE project (color contours). Solid and dotted black lines are the PDFs of the collocated retrieved and in situ measured IWC, respectively. The dash–dotted line is the PDF of height for the collocated in situ data.

aggregate LUT retrieval, which will be the standard SNOWIE IWC retrieval dataset for further cloud analysis. This study shows an advantage of the single-aircraft integration of in situ and remote sensing measurements since we can utilize the collocated in situ measurement to choose the appropriate LUT or mass length relationship in the algorithm to improve the algorithm's overall accuracy.

The retrieved IWC from WCR at the flight level is first compared with the Nevzorov IWC measurement from all in-cloud data collected during the SNOWIE project to provide a statistical comparison. During the 3-month SNOWIE project, there are about 75 h of collocated WCR and in situ measurements. To illustrate the data sample representativity, Fig. 3 shows the probability density function (PDF) of the WCR-retrieved IWC by height for the entire SNOWIE project and the PDFs of the collocated retrieved and in situ measured IWC at the flight level. The SNOWIE clouds are mainly around 2–6 km. The clouds below 3.5 km, which are generally in the boundary layer clouds, have dominated IWCs at 0.1 g m^{-3}, whereas the clouds above 3.5 km have mean IWCs decreasing from 0.1 to about 10^{-3} g m^{-3} with increasing heights. The UWKA mainly sampled the clouds over 3–5.5 km. The sampled IWCs from WCR retrieval and Nevzorov measurement at flight level have very similar PDFs, which range from 10^{-4} to 1 g m^{-3} and peak at 0.1 m^{-3}. Given the large amount of sampling volume over different cloud heights (or temperature) and a large IWC value range, the collocated IWC dataset is representative of the cloud properties over the SNOWIE project. The validation results at the flight level should hold for the clouds over the entire project.

Following the statistical analysis, two case studies are presented to show the algorithm performance in different cloud microphysical and dynamic environments. We also present in situ particle size distribution (PSD), forward-simulated Ze and IWC with in situ PSD, and particle images from the optical array probes to explore potential causes of the disagreement between the WCR-retrieved IWC and the in situ measurements.

a. Statistical results of in situ comparison

For direct comparison with in situ measurements, the WCR-retrieved IWC within 300 m of the flight level in each radar profile is averaged, providing a single, "mean flight level" value. Sensitivity tests were conducted to explore the appropriate range for averaging. The sensitivity of mean flight level value to 250- and 500-m averages is relatively small in comparison with the standard deviation due to the cloud variation within the 300 m. The Nevzorov data are saved at 1 Hz. The WCR retrieval is recorded at 2 Hz. So the Nevzorov data are interpolated to WCR time resolution. Then both data have a running smoothing of 5 s.

The 1–1 scatterplot of retrieved mean IWC versus in situ Nevzorov IWC for the entire SNOWIE project is shown in Fig. 4a. The rr between the retrieved and in situ IWCs is 0.88, and the mean bias (defined as IWC_ret − IWC_insitu) is less than 0.05 g m^{-3}, or less than 40%. To further evaluate the algorithm performance in ice clouds or mixed phase clouds, we separate the data with ice fraction ratio (IFR; =IWC/TWC) obtained from the Nevzorov probe. For ice or ice-dominated clouds with IFR $>$ 0.8 shown in Figs. 4d–f, rr is 0.91, the mean bias is close to 0.0, and the IWC ratio (defined as IWC_ret/IWC_insitu) is close to 1. For mixed-phase clouds with IFR $<$ 0.8 shown in Figs. 4g–i, rr decreases to 0.76, and the retrieved IWCs are positively biased by up to 80% when IWCs are less than 0.6 g m^{-3}.

The strong correlation and a bias of close to 0 between retrieved IWC and in situ measured IWC for ice or ice-dominated clouds demonstrates the algorithm validity for these cloud conditions. However, the retrieval is biased large as the cloud liquid water content fraction increases. This discrepancy could be related to the increasing uncertainty of the Nevzorov probe measurement in mixed-phase clouds as discussed in the section 2, particularly in icing conditions, cloud inhomogeneities and the algorithm's inability to account for possible ice particle habit transition in the presence of liquid hydrometeors. These three factors for the IWC discrepancy are investigated in the following case studies.

b. Cases studies

The dominant weather patterns of the SNOWIE intensive observation periods (IOPs) are summarized in Tessendorf et al. (2019). Briefly, clouds encountered during SNOWIE were orographically forced as easterly moving air was forced up and over the mountains of southwestern Idaho. Figures 5 and 6 show two flight legs of WCR and WCL measurements, WCR-retrieved IWC, and collocated in situ comparison for the SNOWIE IOP 8 on 22 January 2017. The IOP 8 is associated with an atmospheric river event off the Pacific Ocean with a deep band of moist air flowing from the Pacific across the Sierra Nevada/Cascade Range and over the low-level blocked flow near the Payette basin. From satellite imagery

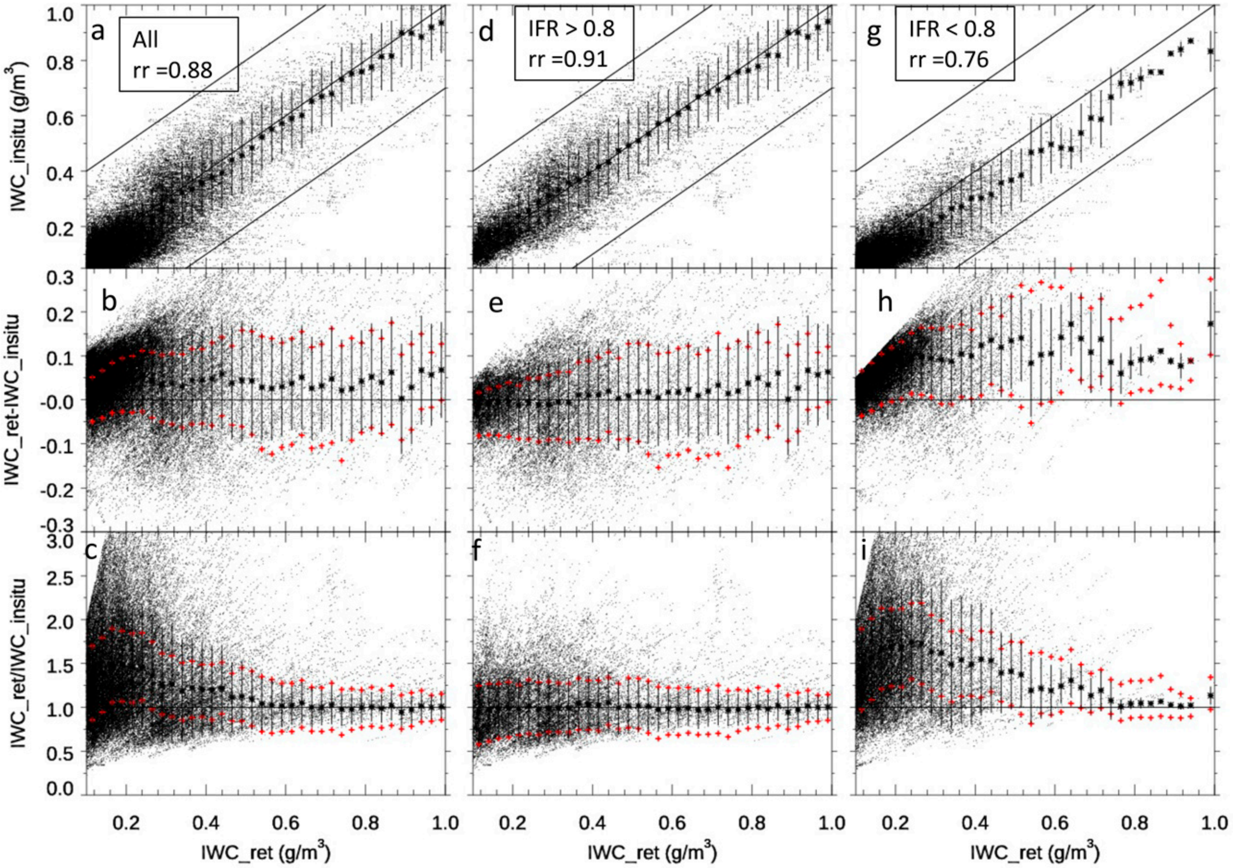

FIG. 4. Comparison of WCR-retrieved mean IWC within 300 m of the flight level with in situ Nevzorov measured IWC for the SNOWIE project in (top) 1–1 scatterplot, (middle) bias, and (bottom) relative ratio for (a)–(c) all clouds and clouds with IFR (d)–(f) larger than or (g)–(i) less than 0.8. The black asterisk and vertical bar are the mean and standard deviation. The red plus in the bias and ratio panels represents the upper and lower limits of 1 standard deviation of the retrieved IWC within 300 m of the flight level. The correlation coefficients (rr) of the retrieved IWC with in situ IWC for all clouds, clouds with IFR $>$ 0.8, and clouds with IFR $<$ 0.8 are 0.88, 0.91, and 0.76, respectively.

(not shown), upper cloud layers were a continuation of upper-tropospheric synoptic ascent into the Payette, while lower cloud layers appeared to be forced by low-level ascent over the Payette. Vertical merger of radar echoes occurred when ice precipitated from the upper into the lower layer, effectively seeding the lower layer. Cloud-top-generating cells (Keeler et al. 2016) were observed at both the lower layer and the upper layer. Updrafts associated with these generating cells, together with warm cloud-top temperatures, often led to SLW near the cloud top of the lower layer during these conditions. The low-level air over the upwind plain was blocked by the mountains and was often very stable because of a sustained inversion, so clouds that formed in this low-level air mass often remained very shallow.

1) CASE 1: ONE MIXED THICK LAYER

The flight leg shown in Fig. 5 sampled a thick layer cloud readily apparent from WCR reflectivity (Fig. 5b) which extended from the mountain top (~2 km) to above 6 km above mean sea level (MSL). The time on the *x* axis in Fig. 5 is reversed so that upstream is on the left. At the upstream end of this leg, there are three separate layers: a lower layer within 2 km of the surface (which, according to radiosonde data, was highly stratified) and a middle layer at 4 km (which was close to moist neutral). There was also a thin layer above 6 km with very weak echoes. The gradually attenuated downward WCL backscattering power (Fig. 5c) and large LDR around 0.5 (Fig. 5d) during 2123–2126, 2133–2135, and 2136–2138 UTC indicated that the cloud was dominated by ice crystals. During 2126:35–2127:35 and 2131:35–2132:15 UTC (which is highlighted in the blue box in Fig. 5), the lidar backscattering power sporadically quickly attenuated within ~100 m, with small LDR around 0.1, which indicated the existence of pockets of numerous small cloud droplets.

The time series of IWC in Fig. 5e shows that the retrieved IWC near the aircraft and in situ IWC have a range of 0.05–0.5 g m^{-3} and a strong correlation with each other. The sampled clouds around 2127 and 2132 UTC (highlighted in blue boxes) have large variances in IWC, and large deviations

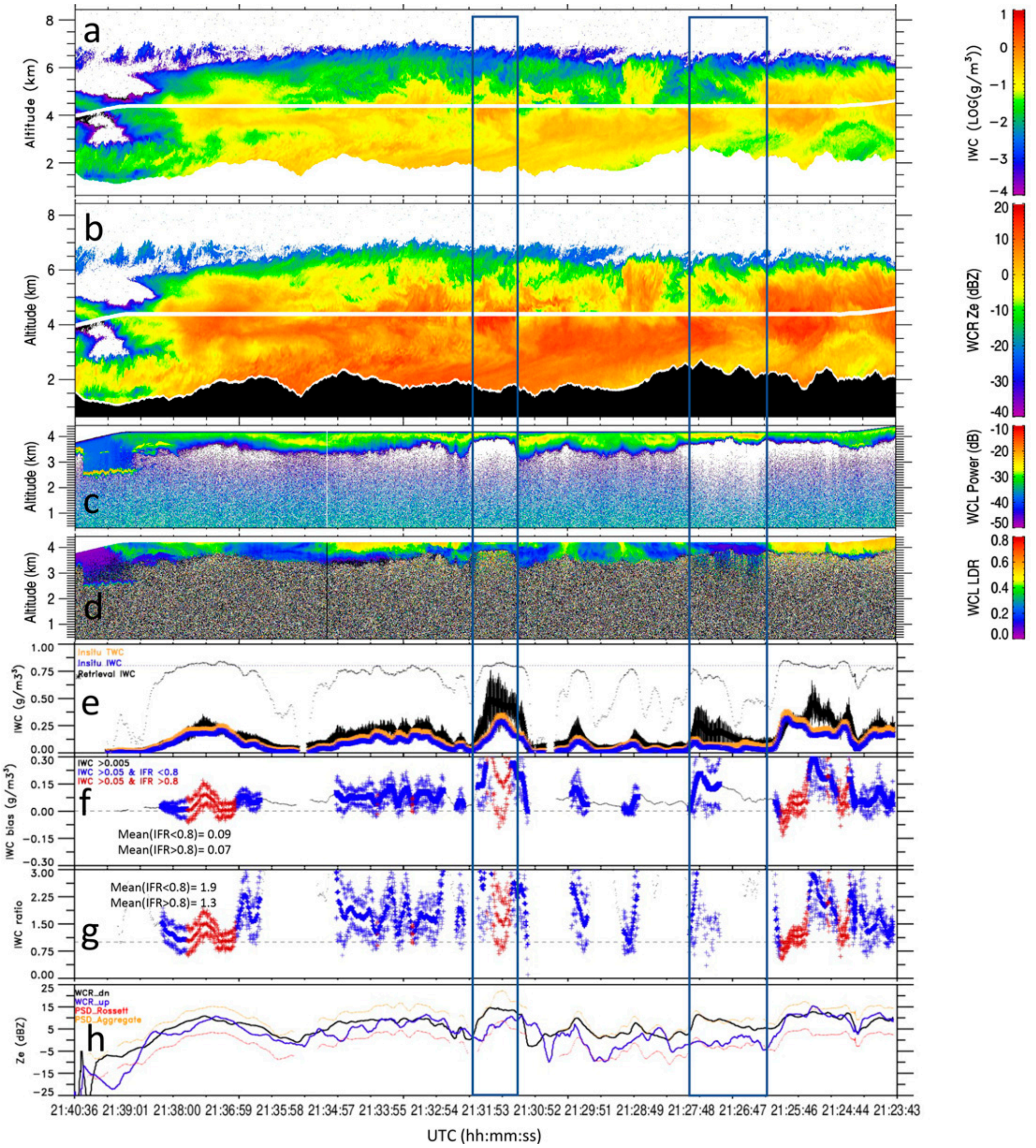

FIG. 5. (a) WCR radar reflectivity, (b) downward WCL backscattering power, (c) lidar depolarization ratio, (d) WCR-retrieved IWC, and (e) time series of retrieved and in situ IWC at flight level. The thick black line with vertical error bars in (e) is mean retrieved IWC, and the thick orange and blue lines are the Nevzorov TWC and IWC, respectively. The thin black dotted line is the IFR. The (f) bias and (g) ratio between the retrieved IWC and in situ IWC. The thin black dot is for data with in situ IWC larger than 0.005 g m^{-3}, the blue and red are for IFR $>$ 0.8 and $<$ 0.8, respectively, and the thick and thin blue plus signs are the mean and the limits of 1 standard deviation, respectively. (h) Mean Ze from WCR up (black) and down (blue) beams. The simulated Ze using PSDs from optical array probes PSDs with bullet rosette and aggregate particle habits are shown as red and orange lines, respectively. The blue-outlined boxes that extend through all panels are discussed in the text.

in IWC ratio (Fig. 5f) and IWC bias (Fig. 5g), apparently related to the cloud inhomogeneity during the clouds mixing. The arithmetic average could be biased as the retrieved IWC distribution is skewed. Nevertheless, the upper and lower limits (blue plus in Figs. 5f,g) of one standard deviation of mean retrieved IWC enclosed the 0 bias line and the 1:1 ratio line. The averaged IWC bias and ratio for clouds with IFR $>$ 0.8 are 0.07 g m^{-3} and 1.4, while they are 0.09 g m^{-3} and 1.9 for clouds with IFR $<$ 0.8, respectively.

The OAP PSDs measured by CDP, 2DS, and 2DP are shown in Fig. 7a (IFR $<$ 0.5) and Fig. 7b (IFR $>$0.8). The CDP droplet concentration of small particles ($D < 50$ μm) in clouds with IFR $<$ 0.5 was ~2 orders of magnitude larger than those in ice-dominated clouds with IFR $>$ 0.8. To investigate

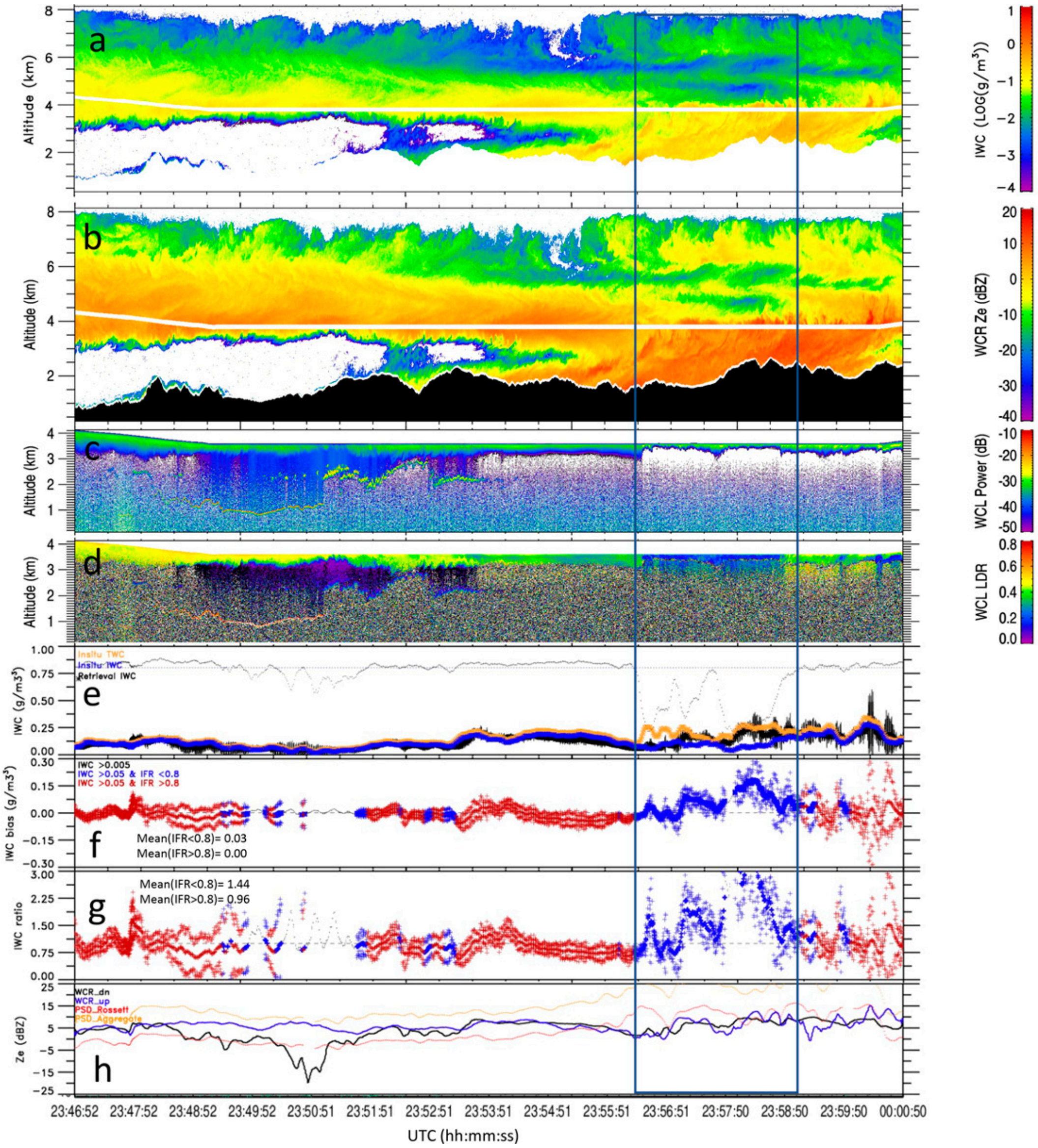

FIG. 6. As in Fig. 5, but for the flight leg at 2348:52 UTC.

the potential impact of liquid droplets on the IWC retrieval, we use that portion of the PSD from the CDP and compute the resulting reflectivity, assuming spherical water droplets (results are not shown). First, the water droplets could have Ze as large as −20 dBZ, which was much less than the WCR observed Ze (0–15 dBZ). Second, the large Ze of water droplets around 2127 and 2132 UTC (highlighted in blue boxes) were well collocated with the region with rapid WCL backscattering attenuation and the smaller LDR, confirming our previous speculation of SLW existence. Further, one expects that high Ze from the water droplets would be correlated with low IFR as it is defined, but the IFR (dotted thin black line in Fig. 5e) is well correlated with IWC except around 2126:35–2127:35 UTC. It was found that the Nevzorov LWC had a constant residue of ~0.02 g m^{-3}, and the regions of low IFR in other regions appear to be more the result of reduced IWC rather than increased LWC.

Figures 7a and 7b also show that the number concentration of large ice particles (Dmax > 100 μm) increased in regions of larger IFR. The simulated Ze using PSDs from 2DS and 2DP assuming bullet rosette and aggregate ice particles are shown in Fig. 5h (red and yellow lines, respectively). For regions of high IFR, the mean Ze of WCR up and down beams were close to each other and match well with that calculated from the PSDs assuming aggregates. For the mixing region during 2126–2133 UTC where IFR is fluctuating, the difference between Ze from the up and down beams is as large as 10 dB, consistent with the large IWC variations within 300 m of the flight level, which indicates that the cloud

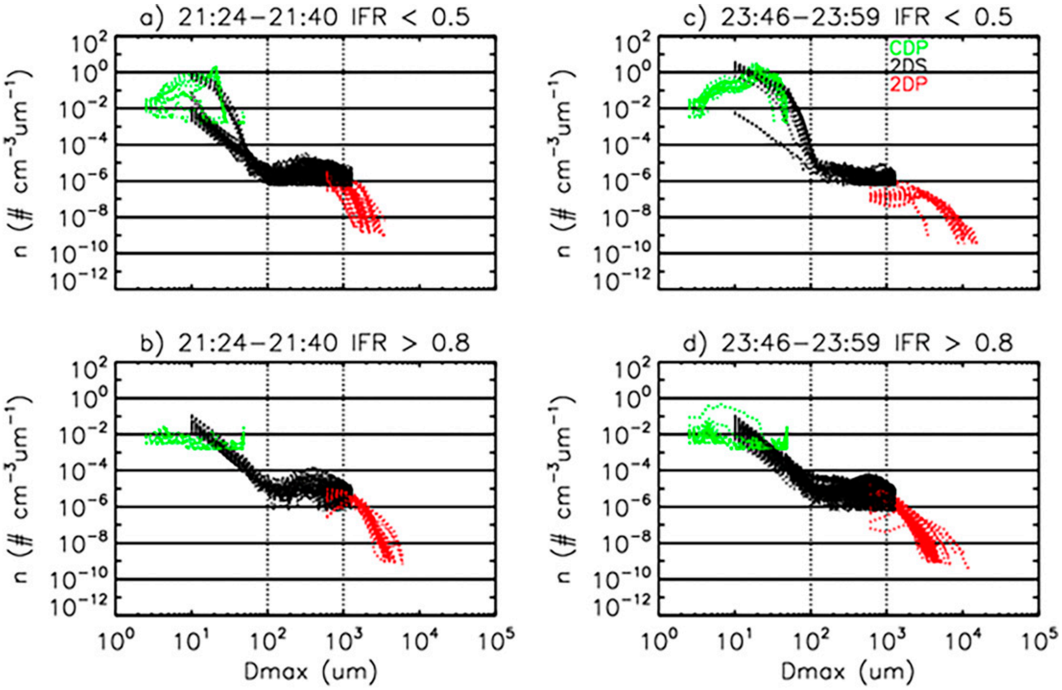

FIG. 7. OAP PSD comparison for (a),(b) the leg during 2124–2140 UTC and the leg during (c),(d) 2346–2359 UTC with (top) IFR < 0.5 and (bottom) IFR > 0.8. Color measurements are from CDP (green), 2DS (black), and 2DP (red).

variation could cause the large standard deviation between the retrieved and in situ IWC.

Figure 8a showed the ice particle images from the 2DS *V* channel for 2126:19 to 2127:37 UTC. Prior to 2126:35 UTC, the ice particle larger than 120 μm in diameter seemed dominated by mostly aggregate-like habit. After that the column-like and bullet rosette–like ice particles increased, then it transitioned to aggregate-like particle after 2127:35 UTC. The WCR retrieval algorithm, assuming a modified gamma PSD of aggregate ice particles, could not count for this habit variation and could cause uncertainty or bias.

2) CASE 2: A BOUNDARY LAYER MERGING INTO AN ELEVATED LAYER

From 2346:52 until 2355:18 UTC the UWKA flew through the base of a 4-km-thick elevated cloud at a flight level of ~4 km, roughly 2 km above the underlying surface (Fig. 6). The cloud had lots of generating cell at the cloud top as shown in Ze and IWC (Figs. 6a,b), which were associated with the frequent and strong updrafts in retrieved Wm (not shown). Below the flight level, the backscattering signal of the downward WCL was gradually attenuated with LDR around 0.4, indicating ice or ice-dominated clouds. Around 2358:18 UTC, a boundary layer cloud became deep and merged with the thick upper-level clouds. This boundary cloud contains greater Ze and IWC, with what appear to be cloud-top cells silhouetted against the weaker upper-level clouds (Figs. 6a,b). At this time the downward WCL backscatter signal became fully attenuated within ~100 m of the flight level and the LDR decreased to around 0.1, indicating the presence of SLW.

Figure 6e shows the time series of retrieved mean IWC around the flight level and in situ measured IWC. Figure 6h shows the averaged Ze sampled by the up and down WCR beams within 300 m of the flight level and simulated Ze from OAP PSDs. For the elevated layer, the Ze from the up and down WCR beams agreed agree well, generally within a few decibels, except for around 2350 UTC when the UWKA passed very near the cloud-base edge. The simulated Ze from water droplets using the CDP measured PSD remained at or below −30 dB*Z*. Around 2350 UTC, the IFR decreased to 0.6 due to the Nevzorov LWC remainder and decreased IWC. Throughout this layer the retrieved IWC agreed very well with the in situ IWC with 0 bias (black line in Fig. 6f). At (and after) about 2356:30 UTC, the UWKA penetrated through the boundary cloud layer. From this time through the end of the leg TWC increased to about 0.25 g m^{-3}, 2 times that encountered in the elevated cloud layer. During 2356:30–2358:45 UTC, the IFR decreased to below 0.3 as the LWC increased from 0.025 to 0.2 g m^{-3}, while the IWC is almost the same. Both up and down WCR mean Ze increases from about 5 dB in the high level cloud to around 10–15 dB*Z* in the boundary layer. The simulated Ze of aggregates increases by more than 10 dB*Z*, which is caused by the increased concentration of large ice particles (shown in Fig. 7c). The retrieved IWC also increases as the WCR Ze increases. However, it was biased larger than the in situ IWC by up to a factor of 2.

a) 2DS V Channel 212619-212737

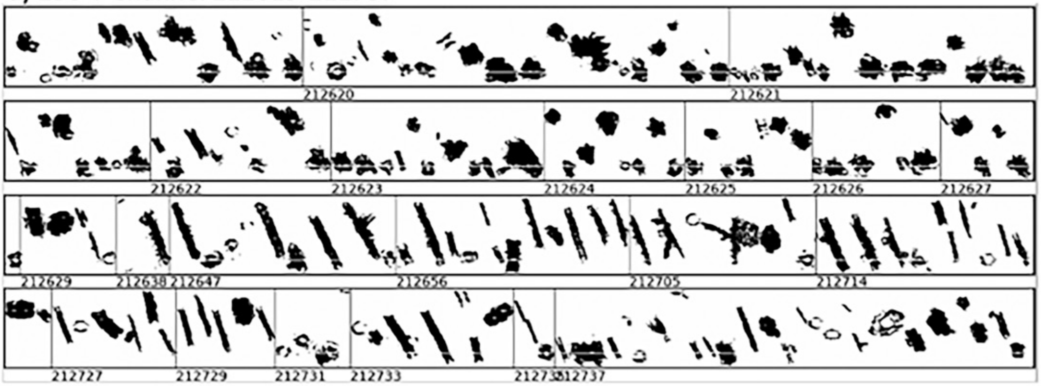

b) 2DS V Channel 235400-235438

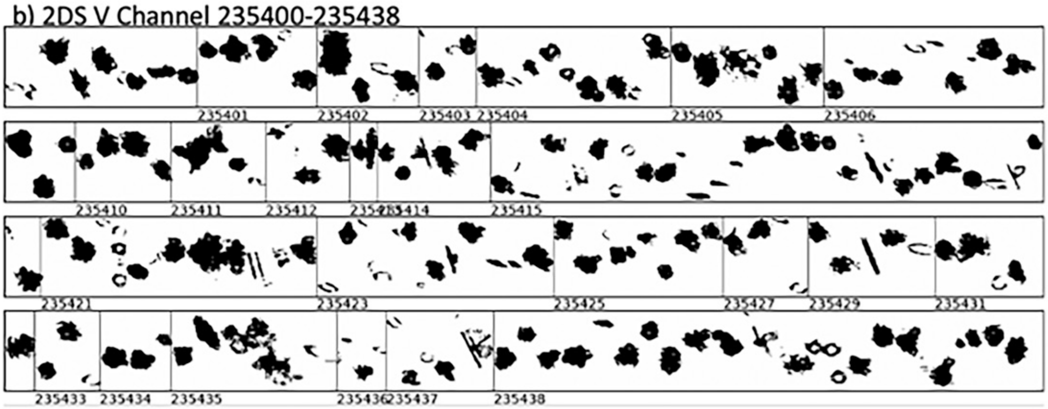

c) 2DS V Channel 235600-235841

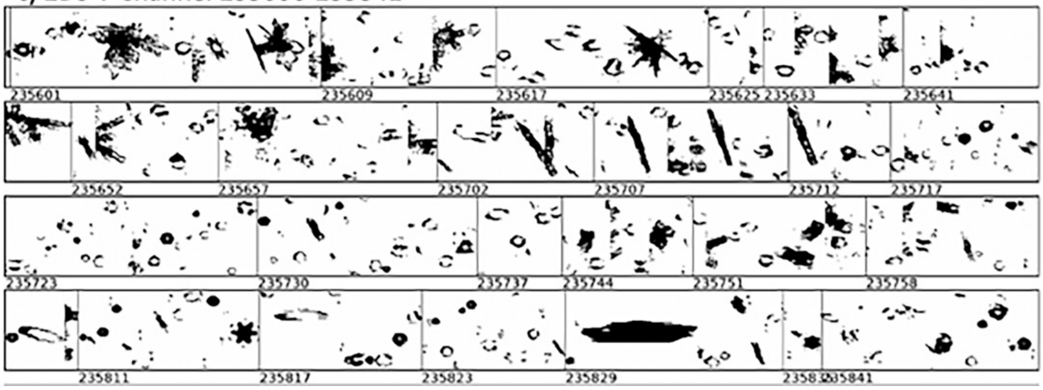

FIG. 8. Two-dimensional stereo probe (2DS) V channel images of particles with Dmax larger than 120 μm for three periods: (a) 2126:19–2127:37, (b) 2354:00–2354:38, and (c) 2356:00–2358:41 UTC.

The OAP PSDs measured by CDP, 2DS and 2DP for this leg are shown Fig. 7c (IFR < 0.5) and Fig 7d (IFR > 0.8). The clouds with IFR < 0.5 had abundant small water droplets, similar to that observed in case 1, with Ze computed from CDP measurements at about -10 dBZ. The number concentration of large ice particles ($100 <$ Dmax <1000 μm) increased in ice-dominated clouds, also similar to case 1, but the water-dominated clouds have an extended tail of larger particles, which causes the simulated PSD Ze of aggregates biased larger than the WCR Ze in Fig. 6h. Figure 8 shows the particle images from the 2DS V channel for the elevated cloud layer (Fig. 8b) and the boundary layer cloud (Fig. 8c). Images that appear to have "holes" are the result of smaller particles that are near the edge of their depth of field and/or larger particles which may allow light transmission through the crystal (Lawson et al. 2006). In the elevated cloud, the ice particles are dominated by aggregates roughly 500 μm in diameter, whereas in the boundary layer cloud there are extremely large bullet rosette–like and column-like ice particles. To be cautious, the name of the observed ice particle

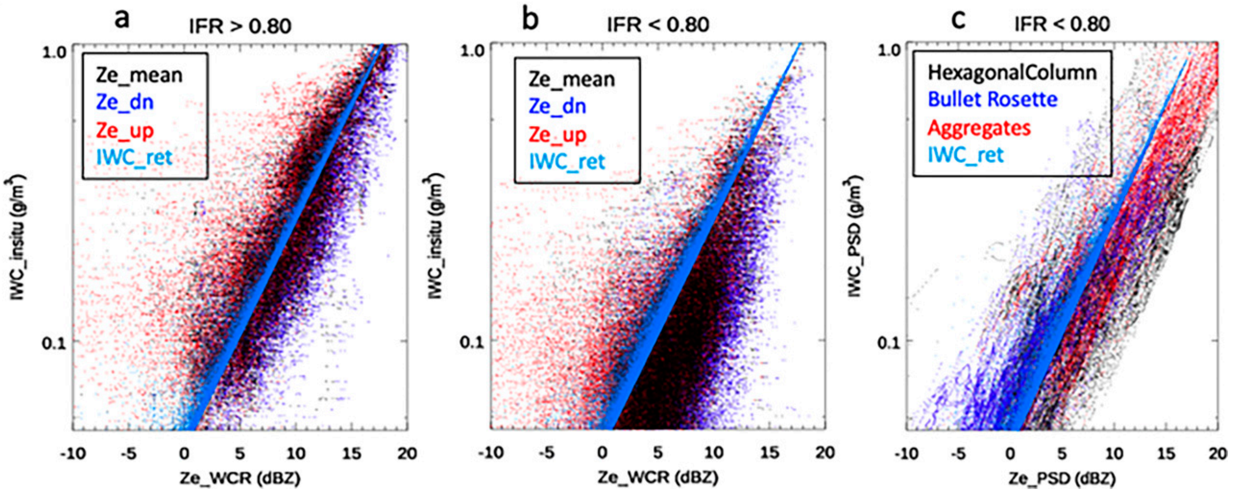

FIG. 9. The Ze–IWC relationship comparison for (a) IFR > 0.8 and (b) IFR < 0.8. In (a) and (b), the mean WCR Ze from both or separate up and down beams vs in situ IWC are plotted in black, red and blue dots, respectively. The WCR Ze_mean vs retrieved IWC is plotted in lighter blue dots. (c) The simulated Ze–IWC relationships of hexagonal column, bullet rosette, and aggregate particles are shown in black, blue, and red dots, respectively, in comparison with the WCR Ze_mean vs retrieved IWC relation in lighter blue.

shape in Fig. 8 is based on the closeness to the shapes assumed in Yang et al. (2005), rather than the aggregation/deposition process.

c. Ze–IWC relationship comparison

To further demonstrate the uncertainties associated with the algorithm assumption of the ice particle habit and the PSD, we simulate the IWC and Ze using the in situ PSD measurements during the entire project, assuming different idealized particle habits, and compare their relations with the in situ measured IWC and WCR measured Ze relation. For this simulation, we use the 2DS measurements for particles with diameters from 75 to 1000 μm and the 2DP measurements for particles with diameters larger than 1000 μm.

The WCR observed Ze and in situ observed IWC are scatterplotted in Figs. 9a and 9b for clouds with IFR > 0.8 and IFR < 0.8, respectively. The WCR mean Ze within the 300 m range and the separate up/down beam averages show the cloud variation: the cloud with IFR< 0.8 had larger cloud variation than the cloud with IFR > 0.8. The Ze–IWC relationship for the retrieval algorithm, assumed aggregate ice particles of modified gamma PDS, is shown in Fig. 9 in lighter blue dots. For clouds with IFR > 0.8, the observed Ze–IWC are scattered around the retrieval Ze–IWC, while for clouds with IFR < 0.8, the observed mean Ze–IWC are skewed to the right of the retrieval Ze–IWC. This comparison pattern is consistent with the IWC comparison in Figs. 4d and 4g.

The PSD simulated Ze–IWC relations of three idealized ice particle habits from all PSD measurements during the entire SNOWIE project are shown in Fig. 9c. The PSD Ze–IWC relation for each habit has a large scattering relative to the retrieval Ze–IWC relation, due to the PSD shape discrepancy or the measured PSD size incompleteness, which has been shown in previous studies (Deng and Mace 2006). Second, the difference among the habits is obvious. The IWC of hexagonal column of the same Ze is smaller than the aggregates as shown by the mass–length relation in Fig. 1a. The PSD Ze–IWC of hexagonal columns is more similar to the observed Ze–IWC in water-dominated clouds, which is consistent with the 2DS images of the prevalence of large column-like particles. This habit change in different types of clouds could not be accounted in the retrieval algorithm and results in certain bias as shown in Fig. 4g.

5. Discussion and summary

The vertical structures of ice microphysical properties and air vertical motion are complementary to the in situ data for the cloud-microphysical processes within a cloud layer or between multiple layers of clouds. The IWC and LWC variations in the orographic winter storm are strongly related to the dynamic structure revealed in WCR transects. Therefore, the WCR retrieval extends the in situ measurements from the flight level to the whole vertical profile, and sheds light on the impact of air dynamics on cloud-microphysical processes in mixed phase clouds that form and enhance cloud and precipitation in natural cloud formation and artificial cloud seeding events.

We present an algorithm for the retrieval of IWC and Wm from millimeter-wave radar reflectivity and Doppler velocity profiles in ice and mixed-phase clouds. The algorithm assumes clouds are ice dominated, or at least, the reflectivity can be attributed exclusively to ice particles or snow, and liquid attenuation is ignored. The ice particle habit evolution during the cloud process is not accounted for in the algorithm since the algorithm assumes certain particle habit for all clouds.

The retrieval algorithm is ill conditioned and benefits from an accurate first guess and an accurate ice particle habit assumption. In the case presented herein, an airborne radar is used, and the first-guess IWC and habit information are obtained from proximity-flight-level microphysical probe data. The resulting retrieved IWC in ice-dominated clouds agrees well with in situ measurements, with a correlation coefficient of 0.91 and a near-zero mean bias.

Liquid-dominated clouds and clouds with low IWC yield larger departures and biases of retrieved IWC from in situ measurements. Such a discrepancy is found to be related to the Nevzorov LWC–TWC probe uncertainty, the large vertical inhomogeneity, and the algorithm assumption uncertainty. The in situ PSD and 2DS images in clouds with significant SLW showed increased number concentration of small droplets and bullet rosette–like and hexagonal column–like large ice particles. The assumed Ze–IWC relation of modified gamma PSD of aggregate particles in the retrieval is biased larger than the WCR Ze and in situ IWC relation in those clouds. The PSD simulated Ze–IWC relationship with three idealized ice particle habits showed that hexagonal column particles with the same Ze have lower IWC than aggregates, which seems consistent with the WCR Ze and in situ IWC relation and the 2DS images, indicating that rapid ice particle habit changes may occur at a constant elevation in orographic mixed-phase clouds.

This WCR retrieval study demonstrates that the UWKA measurements with a suite in situ and remote sensing measurements provide a unique dataset for algorithm development and evaluation, not only for UWKA remote sensing measurements itself, but also for satellite remote sensing measurements. Take the *CloudSat* 2C-ICE retrieval, for example: so far it has been evaluated by limited in situ measurements (1500 sampling points) over the entire Small Particles in Cirrus (SPARTICUS) projects. Their temporal and spatial collocation varies by as much as 20 min and ~3 km (Deng et al. 2013). For future satellite validation projects, such as the Atmosphere Observing System mission, we can think about using UWKA or similar aircraft with integrated in situ and remote sensing measurements with a two-step method. First, we can use the flight level in situ data to validate the aircraft remote sensing retrieval. Then we can use the validated aircraft retrieval data to validate the satellite retrieval data. In such a way, the retrieval at flight level and in situ data has better temporal and special collocations than the collocated data between in situ and satellite data, given the same aircraft flight time. Moreover, the well-validated retrieval data from the aircraft remote sensing measurements will provide a larger sample data volume for satellite remote sensing algorithm development and alleviate the collocation and sampling error between the in situ and satellite measurements.

Acknowledgments. We thank the crews from the University of Wyoming King Air for operating and deploying instruments during the campaign and for data processing after the campaign. We acknowledge the funding support through the cooperative agreement from the National Science Foundation. We thank the anonymous reviewers for their comments and suggestions.

Data availability statement. The SNOWIE remote sensing and in situ measurement data are publicly available from the UWKA project (http://www.atmos.uwyo.edu/uwka/projects/index.shtml) and the SNOWIE project data site from NCAR EOL (https://data.eol.ucar.edu/master_lists/generated/snowie/), which is maintained by the Earth Observing Laboratory at NCAR. The DOIs of the flight data, Nevzorov, OAP, WCR, and WCL data are in the reference list (French and Majewksi 2017; French and Behringer 2021; Research Flight Center 2017a,b,c).

REFERENCES

Brenguier, J.-L., and Coauthors, 2013: In situ measurements of cloud and precipitation particles. *Airborne Measurements for Environmental Research: Methods and Instruments*, A. Kokhanovsky, M. Wendisch, and J.-L. Brenguier, Eds., John Wiley and Sons, 225–301, https://doi.org/10.1002/9783527653218.ch5.

Comstock, J. M., A. Protat, and S. A. McFarlane, 2013: Assessment of uncertainty in cloud radiative effects and heating rates through retrieval algorithm differences: Analysis using 3 years of ARM data at Darwin, Australia. *J. Geophys. Res. Atmos.*, **118**, 4549–4571, https://doi.org/10.1002/jgrd.50404.

Deng, M., and G. G. Mace, 2006: Cirrus microphysical properties and air motion statistics using cloud radar Doppler moments. Part I: Algorithm description. *J. Appl. Meteor. Climatol.*, **45**, 1690–1709, https://doi.org/10.1175/JAM2433.1.

——, ——, Z. Wang, and R. P. Lawson, 2013: Evaluation of several A-Train ice cloud retrieval products with in situ measurements collected during the SPARTICUS campaign. *J. Appl. Meteor. Climatol.*, **52**, 1014–1030, https://doi.org/10.1175/JAMC-D-12-054.1.

Faber, S., J. R. French, and R. C. Jackson, 2018: Laboratory and in-flight evaluation of measurement uncertainties from a commercial cloud droplet probe (CDP). *Atmos. Meas. Tech.*, **11**, 3645–3659, https://doi.org/10.5194/amt-11-3645-2018.

Field, P. R., A. J. Heymsfield, and A. Bansemer, 2006: Shattering and particle interarrival times measured by optical array probes in ice clouds. *J. Atmos. Oceanic Technol.*, **23**, 1357–1371, https://doi.org/10.1175/JTECH1922.1.

Finlon, J. A., G. M. McFarquhar, R. M. Rauber, D. M. Plummer, B. F. Jewett, D. Leon, and K. R. Knupp, 2016: A comparison of X-band polarization parameters with in situ microphysical measurements in the comma head of two winter cyclones. *J. Appl. Meteor.*, **55**, 2549–2574, https://doi.org/10.1175/JAMC-D-16-0059.1.

French, J. R., and A. Majewksi, 2017: UW King Air hydrometeor size spectra data, version 1.0. UCAR/NCAR Earth Observing Laboratory, accessed 5 May 2021, https://doi.org/10.5065/D6GT5KXK.

——, and D. Behringer, 2021: UW King Air manually corrected Nevzorov liquid/total/ice water content, version 1.0. UCAR/NCAR Earth Observing Laboratory, accessed 20 December 2021, https://doi.org/10.26023/2QRK-XSBA-RS0P.

——, and Coauthors, 2018: Precipitation formation from orographic cloud seeding. *Proc. Natl. Acad. Sci. USA*, **115**, 1168–1173, https://doi.org/10.1073/pnas.1716995115.

Friedrich, K., and Coauthors, 2021: Microphysical characteristics and evolution of seeded orographic clouds. *J. Appl. Meteor. Climatol.*, **60**, 909–934, https://doi.org/10.1175/JAMC-D-20-0206.1.

Geerts, B., Q. Miao, and Y. Yang, 2011: Boundary layer turbulence and orographic precipitation growth in cold clouds:

Evidence from profiling airborne radar data. *J. Atmos. Sci.*, **68**, 2344–2365, https://doi.org/10.1175/JAS-D-10-05009.1.

Grasmick, C., and B. Geerts, 2020: Detailed dual-Doppler structure of Kelvin–Helmholtz waves from an airborne profiling radar over complex terrain. Part I: Dynamic structure. *J. Atmos. Sci.*, **77**, 1761–1782, https://doi.org/10.1175/JAS-D-19-0108.1.

Haimov, S., and A. Rodi, 2013: Fixed-antenna pointing-angle calibration of airborne Doppler cloud radar. *J. Atmos. Oceanic Technol.*, **30**, 2320–2335, https://doi.org/10.1175/JTECH-D-12-00262.1.

Heymsfield, A. J., and J. Iaquinta, 2000: Cirrus crystal terminal velocities. *J. Atmos. Sci.*, **57**, 916–938, https://doi.org/10.1175/1520-0469(2000)057<0916:CCTV>2.0.CO;2.

——, and Coauthors, 2008: Testing IWC retrieval methods using radar and ancillary measurements with in situ data. *J. Appl. Meteor. Climatol.*, **47**, 135–163, https://doi.org/10.1175/2007JAMC1606.1.

Hong, G., 2007: Radar backscattering properties of nonspherical ice crystals at 94 GHz. *J. Geophys. Res.*, **112**, D22203, https://doi.org/10.1029/2007JD008839.

Jackson, R. C., G. M. McFarquhar, J. Stith, M. Beals, R. A. Shaw, J. Jensen, H. Fugal, and A. Korolev, 2014: An assessment of the impact of antishattering tips and artifact removal techniques on cloud ice size distributions measured by the 2D cloud probe. *J. Atmos. Oceanic Technol.*, **31**, 2567–2590, https://doi.org/10.1175/JTECH-D-13-00239.1.

Keeler, J. M., B. F. Jewett, R. M. Rauber, G. M. McFarquhar, R. M. Rasmussen, L. Xue, C. Liu, and G. Thompson, 2016: Dynamics of cloud-top generating cells in winter cyclones. Part II: Radiative and instability forcing. *J. Atmos. Sci.*, **73**, 1529–1553, https://doi.org/10.1175/JAS-D-15-0127.1.

Kikuchi, M., H. Okamoto, and K. Sato, 2021: A climatological view of horizontal ice plates in clouds: Findings from nadir and off-nadir *CALIPSO* observations. *J. Geophys. Res. Atmos.*, **126**, e2020JD033562, https://doi.org/10.1029/2020JD033562.

Korolev, A. V., and J. W. Strapp, 2002: Accuracy of measurements of cloud ice water content by the Nevzorov probe. *40th AIAA Aerospace Sciences Meeting and Exhibit*, Reno, NV, AIAA, AIAA-2002-0679, https://doi.org/10.2514/6.2002-679.

——, A. N. Nevzorov, J. W. Strapp, and G. A. Isaac, 1998: The Nevzorov airborne hot-wire LWC–TWC probe: Principle of operation and performance characteristics. *J. Atmos. Oceanic Technol.*, **15**, 1495–1510, https://doi.org/10.1175/1520-0426(1998)015,1495:TNAHWL.2.0.CO;2.

——, E. Emery, and K. Creelman, 2013a: Modification and tests of particle probe tips to mitigate effects of ice shattering. *J. Atmos. Oceanic Technol.*, **30**, 690–708, https://doi.org/10.1175/JTECH-D-12-00142.1.

——, J. W. Strapp, G. A. Isaac, and E. Emery, 2013b: Improved airborne hot-wire measurements of ice water content in clouds. *J. Atmos. Oceanic Technol.*, **30**, 2121–2131, https://doi.org/10.1175/JTECH-D-13-00007.1.

Lance, S. C. A., 2010: Water droplet calibration of the cloud droplet probe (CDP) and in-flight performance in liquid, ice and mixed-phase clouds during ARCPAC. *Atmos. Meas. Tech.*, **3**, 1683–1706, https://doi.org/10.5194/amt-3-1683-2010.

Lawson, R. P., D. O'Connor, P. Zmarzly, K. Weaver, B. A. Baker, Q. Mo, and H. Jonsson, 2006: The 2D-S (stereo) probe: Design and preliminary tests of a new airborne, high speed, high-resolution particle imaging probe. *J. Atmos. Oceanic Technol.*, **23**, 1462–1477, https://doi.org/10.1175/JTECH1927.1.

Leroy, D., and Coauthors, 2017a: Ice crystal sizes in high ice water content clouds. Part II: Statistics of mass diameter percentiles in tropical convection observed during the HAIC/HIWC project. *J. Atmos. Oceanic Technol.*, **34**, 117–136, https://doi.org/10.1175/JTECH-D-15-0246.1.

——, L. Lilie, M. Weber, A. Schwarzenboeck, and W. Strapp, 2017b: ROBUST hot wire probe efficiency for total water content measurements in glaciated conditions. *EGU General Assembly*, Vienna, Austria, EGU, 13217.

Matrosov, S. Y., A. V. Korolev, and A. J. Heymsfield, 2002: Profiling cloud ice mass and particle characteristic size from Doppler radar measurements. *J. Atmos. Oceanic Technol.*, **19**, 1003–1018, https://doi.org/10.1175/1520-0426(2002)019<1003:PCIMAP>2.0.CO;2.

——, M. D. Shupe, A. J. Heymsfield, and P. Zuidema, 2003: Ice cloud optical thickness and extinction estimates from radar measurements. *J. Appl. Meteor.*, **42**, 1584–1598, https://doi.org/10.1175/1520-0450(2003)042<1584:ICOTAE>2.0.CO;2.

Mitchell, D. L., 1996: Use of mass- and area-dimensional power laws for determining precipitation particle terminal velocities. *J. Atmos. Sci.*, **53**, 1710–1723, https://doi.org/10.1175/1520-0469(1996)053<1710:UOMAAD>2.0.CO;2.

Rauber, R. M., and Coauthors, 2019: Wintertime orographic cloud seeding—A review. *J. Appl. Meteor. Climatol.*, **58**, 2117–2140, https://doi.org/10.1175/JAMC-D-18-0341.1.

Research Flight Center, 2017a: Flight level data from the University of Wyoming King Air during the Seeded and Natural Orographic Wintertime clouds: The Idaho Experiment (SNOWIE) project, version 1.0. University of Wyoming Dept. of Atmospheric Science, accessed 11 January 2021, https://doi.org/10.15786/M2MW9F.

——, 2017b: Wyoming Cloud Radar data from the University of Wyoming King Air during the University of Wyoming King Air during the Seeded and Natural Orographic Wintertime clouds: The Idaho Experiment (SNOWIE) project, version 1.0. University of Wyoming Dept. of Atmospheric Science, accessed 11 January 2021, https://doi.org/10.15786/M2CD4J.

——, 2017c: Nadir pointing Wyoming Cloud Lidar (WCL) data from the University of Wyoming King Air during the Seeded and Natural Orographic Wintertime CLOUDS: The Idaho Experiment (SNOWIE) project, version 1.0. University of Wyoming Dept. of Atmospheric Science, accessed 11 January 2021, https://doi.org/10.15786/M2H66G.

Rodgers, C. D., 2000: *Inverse Methods for Atmospheric Sounding: Theory and Practice.* Series on Atmospheric Oceanic and Planetary Physics, Vol. 2, World Scientific, 238 pp.

Skolnick, M., 2008: *Radar Handbook.* 3rd ed. McGraw-Hill, 1328 pp.

Strapp, J. W., L. E. Lilie, E. Emery, and D. Miller, 2005: Preliminary comparison of ice water content as measured by hot wire instruments of varying configuration. *43rd AIAA Aerospace Sciences Meeting and Exhibit*, Reno, NV, AIAA, AIAA 2005-860, https://doi.org/10.2514/6.2005-860.

Tessendorf, S. A., and Coauthors, 2019: A transformational approach to winter orographic weather modification research: The SNOWIE project. *Bull. Amer. Meteor. Soc.*, **100**, 71–92, https://doi.org/10.1175/BAMS-D-17-0152.1.

Vidaurre, G., J. Hallett, and D. C. Rogers, 2011: Airborne measurement of liquid and total water content. *J. Atmos. Oceanic Technol.*, **28**, 1088–1103, https://doi.org/10.1175/JTECH-D-10-05035.1.

Wang, Z., P. Wechsler, W. Kuestner, J. French, A. Rodi, B. Glover, M. Burkhart, and D. Lukens, 2009: Wyoming Cloud Lidar: Instrument description and applications. *Opt. Express*, **17**, 13 576–13 587, https://doi.org/10.1364/OE.17.013576.

——, and Coauthors, 2012: Single aircraft integration of remote sensing and in situ sampling for the study of cloud microphysics and dynamics. *Bull. Amer. Meteor. Soc.*, **93**, 653–668, https://doi.org/10.1175/BAMS-D-11-00044.1.

Yang, P., K. N. Liou, K. Wyser, and D. Mitchell, 2000: Parameterization of scattering and absorption properties of individual ice crystals. *J. Geophys. Res.*, **105**, 4699–4718, https://doi.org/10.1029/1999JD900755.

——, H. Wei, H.-L. Huang, B. A. Baum, Y. X. Hu, G. W. Kattawar, M. I. Mishchenko, and Q. Fu, 2005: Scattering and absorption property database for nonspherical ice particles in the near- through far-infrared spectral region. *Appl. Opt.*, **44**, 5512–5523, https://doi.org/10.1364/AO.44.005512.

Zhao, C., and Coauthors, 2012: Toward understanding of differences in current ARM ground-based cloud retrievals. *J. Geophys. Res.*, **117**, D10206, https://doi.org/10.1029/2011JD016792.